Structural and Dynamic Impacts of Single-atom Disruptions to Guide RNA Interactions within the Recognition Lobe of *Geobacillus stearothermophilus* Cas9

Helen B. Belato[1,#], Alexa L. Knight[1,#], Alexandra M. D'Ordine[1], Chinmai Pindi,[2] Zhiqiang Fan[2], Jinping Luo[2], Giulia Palermo,[2] Gerwald Jogl[1], George P. Lisi[1,4]*

[1]Department of Molecular Biology, Cell Biology & Biochemistry, Brown University, Providence, RI USA

[2]Departments of Bioengineering and Chemistry, University of California Riverside, Riverside, CA USA

[3]Brown University Transgenic Mouse & Gene Targeting Facility, Providence, RI USA

[4]Brown University RNA Center, Providence, RI USA

[#]These authors contributed equally to this work

*** Correspondence:**
george_lisi@brown.edu

Keywords: CRISPR-Cas9, guide RNA, protein dynamics, NMR, thermophile

Abstract

The intuitive manipulation of specific amino acids to alter the activity or specificity of CRISPR-Cas9 has been a topic of great interest. As a large multi-domain RNA-guided endonuclease, the intricate molecular crosstalk within the Cas9 protein hinges on its conformational dynamics, but a comprehensive understanding of the extent and timescale of the motions that drive its allosteric function and association with nucleic acids remains elusive. Here, we investigated the structure and multi-timescale molecular motions of the recognition (Rec) lobe of *Geo*Cas9, a thermophilic Cas9 from *Geobacillus stearothermophilus.* Our results provide new atomic details about the *Geo*Rec subdomains (*Geo*Rec1, *Geo*Rec2) and the full-length domain in solution. Two rationally designed mutants, K267E and R332A, enhanced and redistributed micro-millisecond flexibility throughout *Geo*Rec, and NMR studies of the interaction between *Geo*Rec and its guide RNA showed that mutations reduced this affinity and the stability of the ribonucleoprotein complex.

Despite measured biophysical differences due to the mutations, DNA cleavage assays reveal no functional differences in on-target activity, and similar specificity. These data suggest that guide RNA interactions can be tuned at the biophysical level in the absence of major functional losses but also raise questions about the underlying mechanism of *Geo*Cas9, since analogous single-point mutations have significantly impacted on- and off-target DNA editing in mesophilic *S. pyogenes* Cas9. A K267E/R332A double mutant did also did not enhance *Geo*Cas9 specificity, highlighting the robust tolerance of mutations to the Rec lobe of *Geo*Cas9 and species-dependent complexity of Rec across Cas9 paralogs. Ultimately, this work provides an avenue by which to modulate the structure, motion, and guide RNA interactions at the level of the Rec lobe of *Geo*Cas9, setting the stage for future studies of *Geo*Cas9 variants and their effect on its allosteric mechanism.

Introduction

The vast majority of Cas systems explored as genome editors originate from mesophilic hosts. The emergence of the thermophilic *Geo*Cas9, with DNA cleavage function up to 85°C, can expand CRISPR technology to higher temperature regimes and stabilities,[1,2] but its regulatory mechanism relative to canonical Cas9s must be established. The *Spy*Cas9, which originates from the mesophilic *Streptococcus pyogenes*, as well as *Geo*Cas9, are both effectors of Type-II CRISPR systems. Interestingly, the Type II-A *Spy*Cas9 has been by far the most used Cas enzyme, including in ongoing clinical trials.[3,4] But Cas9 homologs of the Type II-C class, such as *Neisseria meningitis* (*Nme*Cas9) and *Campylobacter jejuni* (*Cje*Cas9), to which *Geo*Cas9 belongs, have been validated for mammalian genome editing,[2,5,6] reinforcing the need to better understand this CRISPR class.

The similar domain arrangements of *Geo*Cas9 and *Spy*Cas9 led us to initially speculate that these could share atomic level mechanistic similarities.[7] *Geo*Cas9 utilizes a guide RNA (gRNA) to localize and unwind a double-stranded DNA (dsDNA) target after recognition of its

51 5'NNNNCRAA-3' protospacer adjacent motif (PAM).[2,8] Upon recognition of the PAM sequence
52 by the PAM-Interacting domain (PI), Cas9-bound guide (gRNA) forms an RNA:DNA hybrid with
53 the target DNA strand. Initially thought to be part of the PI domain[2], the wedge (WED) domain
54 recognizes the repeat:anti-repeat region of the gRNA and the dsDNA upstream of the target
55 region.[9] The Rec lobe of Cas9 is responsible for orienting the RNA:DNA hybrid, as well as the
56 adjacent nuclease domains, into their active conformations.[10-13] Coordinated cleavage of the target
57 and non-target DNA strand then occurs via the HNH and RuvC nucleases, respectively. The
58 *Geo*Cas9 nuclease active sites within HNH and RuvC are spatially distinct from the PAM
59 recognition site in the PI domain, necessitating structural and dynamic changes that allosterically
60 couple dsDNA binding to cleavage. Biochemical[11,14,15] and structural[16,17] experiments using the
61 extensively studied *Spy*Cas9 have revealed that its function is governed by a sophisticated
62 allosteric mechanism that transfers gRNA and dsDNA binding information from the Rec lobe to
63 the distal catalytic sites. A dynamically driven allosteric signal spans the HNH domain of *Spy*Cas9,
64 enabled by the plasticity of the Rec lobe, which orchestrates the conformational activation required
65 for DNA cleavage.[14,18] Our prior work revealed a divergence in the timescales of allosteric motions
66 in the *Spy*Cas9 and *Geo*Cas9 HNH domains[7,17] suggesting an unusually flexible HNH and unique
67 allosteric mode of regulation for *Geo*Cas9. It is therefore also possible that docking of the gRNA
68 with *Geo*Cas9, and thus its interaction with the RNA:DNA hybrid, may differ from the *Spy*Cas9
69 system, as *Geo*Cas9 contains a truncated Rec lobe with only two of the three canonical
70 subdomains.

71 The high thermal stability and more compact size of *Geo*Cas9 (it is 281 residues shorter
72 than *Spy*Cas9) can be especially important for *in vivo* delivery applications, since promising viral
73 vectors (*i.e.* adeno-associated virus, AAV) have cargo capacities of ~4.7kb,[19] which prevents

74 *Spy*Cas9-gRNA packaging into a single AAV vector but permits "all-in-one" delivery of *Geo*Cas9-
75 gRNA.[12] Until the very recent cryo-EM structures of *Geo*Cas9,[20,21] little was known about specific
76 residues that influence its structure, gRNA binding, or function. Our recent NMR work with
77 *Spy*Cas9 uncovered pathways of micro-millisecond timescale motions that propagate chemical
78 information related to allostery and specificity through *Spy*Rec and its RNA:DNA hybrid,[16,17]
79 prompting us to investigate this phenomenon in *Geo*Rec.

80 An atomic-level structural understanding of specificity in large multi-domain protein-
81 nucleic acid complexes like Cas9 is often difficult to address by NMR spectroscopy. Although
82 dynamic ensembles in DNA repair enzymes have provided some insight,[22] many efforts to improve
83 Cas9 specificity and reduce off-target activity have relied on large mutational screens[23] or error-
84 prone PCR[24], which are less intuitive. Inter-subunit allosteric communication between the catalytic
85 HNH domain and the Rec lobe is critical to Cas9 specificity, as the binding of off-target DNA
86 sequences at Rec alter HNH dynamics to affect DNA cleavage.[8,25,26] To further probe the
87 fundamental role of protein motions in the function and specificity of *Geo*Cas9, as well as the
88 effect of protein-nucleic acid interactions on its structural signatures, we engineered two mutations
89 in *Geo*Rec (K267E and R332A, housed within *Geo*Rec2). We hypothesized that these variants
90 could enhance *Geo*Cas9 specificity (*i.e.* limit its off-target cleavage) for two reasons. First, the
91 chosen mutation sites are homologous to those of specificity-enhancing variants of *Spy*Cas9.[24,27]
92 Second, altered Cas9-gRNA interactions have been shown to be a consequence of specificity-
93 enhancement and these charged residues appear to directly interact with the gRNA.[10,11,15,28]
94 Balancing these two points is the fact that Type-II Cas systems generally have conserved nuclease
95 domains, but are delineated by highly varied Rec lobes.[12] This implies that the structural and
96 dynamic properties of Rec may play an outsized role in differentiating the functions of *Spy*Cas9

97 and *Geo*Cas9, which may not be identical. Nevertheless, our work provides new insight into the
98 biophysical, biochemical, and functional role of the *Geo*Rec lobe and how mutations modulate the
99 domain itself and its interaction with gRNA in full-length *Geo*Cas9.

100 **Results**

101 ***The structural similarity of GeoRec1, GeoRec2, and GeoRec facilitates NMR analysis of protein***
102 ***dynamics and RNA affinity***

103 *Geo*Cas9 is a 1087 amino acid polypeptide, thus we employed a "divide and concur"
104 approach for NMR studies, which we previously showed to be useful for quantifying allosteric
105 structure and motion in *Spy*Cas9.[16,17,29,30] The *Geo*Rec lobe is comprised of subdomains *Geo*Rec1
106 and *Geo*Rec2, which likely work together to recognize nucleic acids. We engineered constructs of
107 the *Geo*Rec1 (136 residues, 16 kDa) and *Geo*Rec2 (212 residues, 25 kDa) subdomains and solved
108 the X-ray crystal structure of *Geo*Rec2 at 1.49 Å, which aligns remarkably well with the structure
109 of the *Geo*Rec2 domain within the AlphaFold model (RMSD 1.03 Å) and new cryo-EM structure
110 of *Geo*Cas9 (RMSD 1.10 Å, **Figure 1A**). We were neither able to crystallize *Geo*Rec1 nor full-
111 length *Geo*Cas9 in the apo state, but our *Geo*Rec2 crystal structure represents the structure of the
112 subdomain within the full-length *Geo*Cas9 protein quite well. Our previous studies of *Geo*HNH
113 also show identical superpositions of X-ray crystal structures with full-length Cas complexes.[7] In
114 addition to the individual subdomains, we also generated an NMR construct of the intact *Geo*Rec
115 (370 residues, 43 kDa).

116 Despite only 22% sequence identity, the structure of *Spy*Rec3 and *Geo*Rec2 are highly
117 similar (RMSD 2.00 Å, **Figure S1**). The structure of *Geo*Rec1, in contrast, does not align perfectly
118 with *Spy*Rec1, instead, it partially aligns with both *Spy*Rec1 and *Spy*Rec2 **(Figure S1**). Thus, the
119 nearly identical *Spy*Rec3 and *Geo*Rec2 architectures and their intrinsic dynamics may be a

common thread among Type II Cas9s of different size and PAM preference. To capture atomic-level signatures of *Geo*Rec, we obtained well-resolved ^{1}H-^{15}N NMR fingerprint spectra for all three protein constructs and assigned the amide backbones (**Figure S2**). ^{1}H-^{15}N amide and ^{1}H-$^{13}CH_3$ Ile, Leu, and Val (ILV)-methyl NMR spectra (**Figure 1B, S3**) of *Geo*Rec overlay very well with those of its individual subdomains, suggesting that the linkage of subdomains within the full-

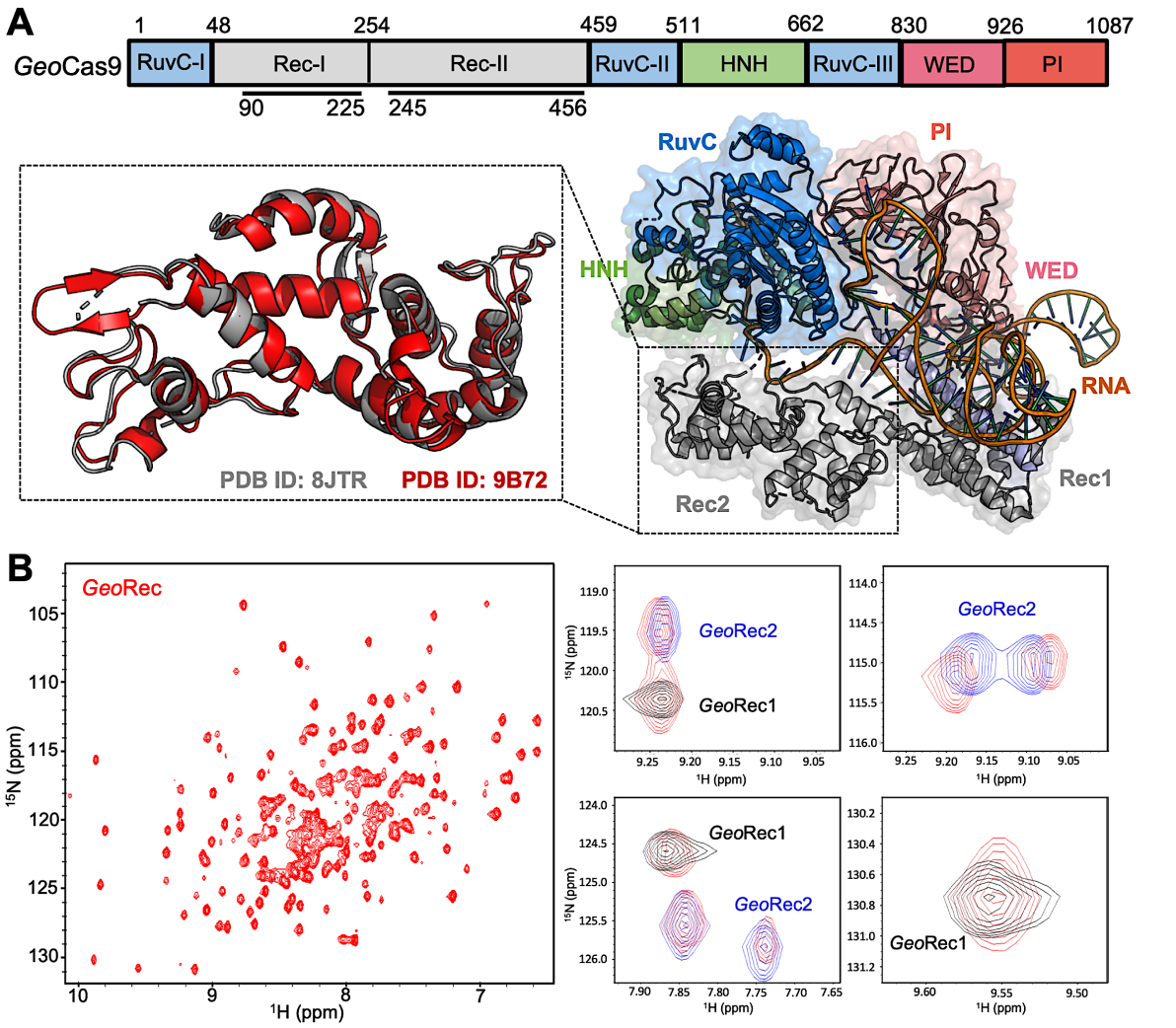

Figure 1. (A) Arrangement of *Geo*Cas9 domains across the primary sequence. The cryo-EM structure of *Geo*Cas9 in complex with gRNA (PDB: 8JTR) shows poor resolution of HNH. The *Geo*Rec2 domain from PDB: 8JTR (gray) is overlaid with our X-ray structure of *Geo*Rec2 (red, PDB: 9B72). **(B)** $^{1}H^{15}N$ TROSY HSQC NMR spectrum of *Geo*Rec collected at 850 MHz. Overlays of this spectrum with resonances from spectra of *Geo*Rec1 (black) and *Geo*Rec2 (blue) demonstrate a structural similarity between the isolated subdomains and intact *Geo*Rec.

length *Geo*Rec polypeptide does not alter their individual folds. Consistent with this observation, circular dichroism (CD) thermal unfolding profiles of *Geo*Rec1 (T_m ~ 34 °C) and *Geo*Rec2 (T_m =

127 61.50 °C) are distinct and occur as separate events in the unfolding profile of *Geo*Rec (**Figure S4**).
128 The dumbbell shape of *Geo*Rec, with its two globular subdomains connected by a short flexible
129 linker, is a likely contributor to these biophysical properties.

130 ***Rationally designed GeoRec2 mutants do not substantially impact the GeoRec structure***

131 To understand how the structure and gRNA interactions of *Geo*Cas9 can be modulated at
132 the level of *Geo*Rec, we engineered two charge-altering point mutants in the *Geo*Rec2 subdomain,
133 K267E and R332A. Based on the AlphaFold2 model of *Geo*Cas9, both of these residues are < 5Å
134 from the bound RNA:DNA hybrid and were predicted to interface with the nucleic acids directly
135 (**Figure 2A/B**). A new experimental cryo-EM structure of *Geo*Cas9 confirmed the interaction
136 between K267 and the gRNA, but does not report a < 5Å interaction of R332 with the gRNA.[31]
137 The rationale for our designed mutations was also that removal of positive charge would weaken
138 the interactions between *Geo*Cas9 and the gRNA, affecting K_d via the electrostatics or dynamics
139 of the *Geo*Rec lobe. Studies of *Spy*Cas9 revealed that interaction of *Spy*Rec3 (analogous to
140 *Geo*Rec2) with its RNA:DNA hybrid triggers conformational rearrangements that allow the
141 catalytic HNH domain to sample its active conformation.[11] Thus, *Spy*Rec3 acts as an allosteric
142 effector that recognizes the RNA:DNA hybrid to activate HNH. Mismatches (*i.e.* off-target DNA
143 sequences) in the target DNA generally prevent *Spy*Rec3 from undergoing the full extent of its
144 required conformational rearrangements, leaving HNH in a "proofreading" state with its catalytic
145 residues too far from the DNA cleavage site. Off-target DNA cleavage by Cas9 remains an area
146 of intense study and substantial effort from various groups has gone into mitigating such
147 effects.[15,23,28,32,33] Indeed, many high-specificity *Spy*Cas9 variants contain mutations within
148 *Spy*Rec3 that increase the threshold for its conformational activation, reducing the propensity for
149 HNH to sample its active state in the presence of off-target DNA sequences.[11,15,23] Studies of

150 flexibility within Rec itself, as well as its gRNA interactions in the presence of mutations, are

151 therefore essential to connecting biophysical properties to function and specificity in related Cas9s.

152 The K267E *Geo*Rec2 variant is sequentially and structurally similar to a specificity enhancing

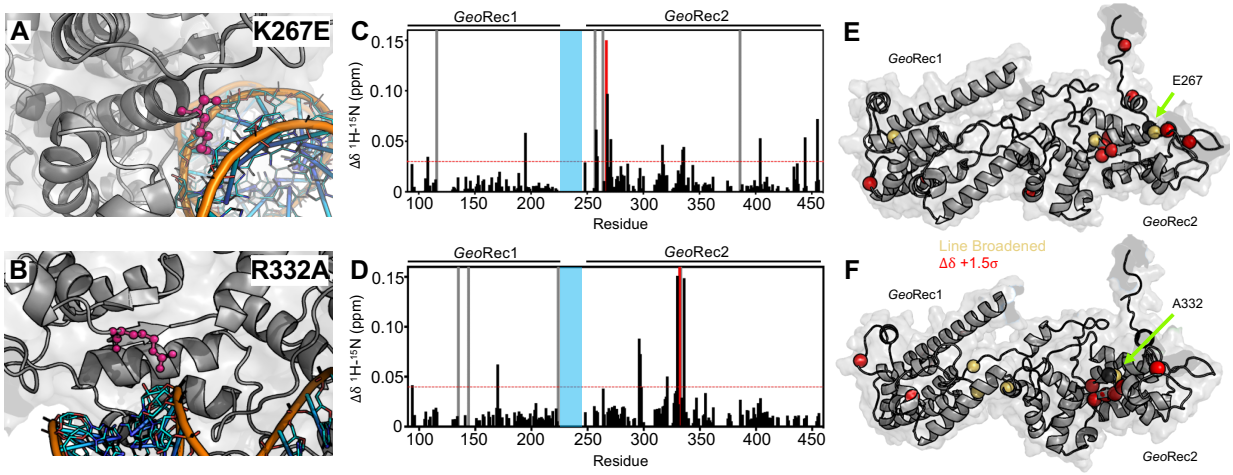

Figure 2. (A, B) Sites of selected mutations within *Geo*Rec2, K267 and R332, are highlighted as purple sticks directly facing the RNA and DNA modeled from *Nme*Cas9 (PDB ID: 6JDV), allowing for prediction of the binding orientation within *Geo*Cas9. NMR chemical shift perturbations caused by the K267E **(C)** or R332A (**D**) mutations are plotted for each residue of *Geo*Rec. Gray bars denote sites of line broadening, the blue bar denotes an unassigned region of *Geo*Rec corresponding to the native Rec1-Rec2 linker, and the red bar indicates the mutation site. The red dashed line indicates 1.5σ above the 10% trimmed mean of the data. Chemical shift perturbations 1.5σ above the 10% trimmed mean are mapped onto K267E **(E)** and R332A **(F)** *Geo*Rec (red spheres). Resonances that have broadened beyond detection are mapped as yellow spheres and the mutation sites are indicated by a black sphere and green arrow.

153 site in *Spy*Cas9 (K526E), within the evoCas9 system.[27] The *Spy*Cas9 K526E mutation substantially

154 reduced off-target activity alone, but was even more effective in conjunction with three other

155 single-point mutations in *Spy*Rec3.[27] The R332A *Geo*Rec2 variant also resembles one mutation

156 within a high-specificity *Spy*Cas9 variant, an early iteration of HiFi *Spy*Cas9 called HiFi Cas9-

157 R691A.[24] We assessed mutation-induced changes to local structure in *Geo*Rec via NMR chemical

158 shift perturbations in ^{1}H-^{15}N HSQC backbone amide spectra. Consistent with experiments using

159 *Geo*Rec2 alone, chemical shift perturbations and line broadening are highly localized to the

160 mutation sites. (**Figure 2C-F**). Perturbation profiles of the *Geo*Rec2 subdomain and intact *Geo*Rec

161 also implicate the same residues as sensitive to the mutations (**Figure S5**).

162 CD spectroscopy revealed that wild-type (WT), K267E, and R332A *Geo*Rec2 maintained
163 similar alpha-helical secondary structure, though the thermostability of both variants was slightly
164 reduced from that of WT *Geo*Rec2 (**Figure S6)**. The T_m of WT *Geo*Rec2 is ~62 °C, consistent
165 with the T_m of the full-length *Geo*Cas9, while that of K267E *Geo*Rec2 was decreased to ~55 °C.
166 Though the R332A *Geo*Rec2 T_m remains ~62 °C, this variant underwent a smaller unfolding event
167 near 40 °C before completely unfolding. These data suggest that despite small structural
168 perturbations, both mutations are destabilizing to *Geo*Rec2, which led us to expect a change in
169 NMR-detectable protein dynamics.

170 ***Mutations enhance and redistribute molecular motions within GeoRec2***

171 Due to the high molecular weight of the intact *Geo*Rec lobe, decays in NMR signal
172 associated with spin relaxation experiments were significant and hampered data quality. Thus, we
173 focused on quantifying the molecular motions of the *Geo*Rec2 subdomain, where the K267E and
174 R332A mutations reside, and the chemical shift perturbations are most apparent. To obtain high-
175 quality per-residue information representative of *Geo*Rec, we measured longitudinal (R_1) and
176 transverse (R_2) relaxation rates and heteronuclear ^{1}H-[^{15}N] NOEs (**Figure S7**), then used these data
177 in a Model-free analysis of per-residue order parameters (S^2). Previous measurements of S^2 across
178 the adjacent *Geo*HNH nuclease revealed substantial ps-ns timescale flexibility,[7] leading us to
179 wonder whether a similar observation would be made for *Geo*Rec2, which abuts *Geo*HNH. Such
180 a finding could suggest that HNH-Rec2 crosstalk in *Geo*Cas9 is driven primarily by rapid bond
181 vector fluctuations. However, unlike *Geo*HNH, S^2 values for *Geo*Rec2 are globally elevated,
182 suggesting that the ps-ns motions of this subdomain arise primarily from global tumbling of the
183 protein in solution. We therefore carried out Carr-Purcell-Meiboom-Gill (CPMG) relaxation
184 dispersion NMR experiments to assess the flexibility of *Geo*Rec2 on slower timescales, which has

been linked to chemical information transfer in the well-studied *Spy*Cas9.[10,16,17,29] Evidence of µs-ms motions (*i.e.* curved relaxation dispersion profiles) is observed in 17 residues within the *Geo*Rec2 core, spanning its interfaces to Rec1 and HNH **(Figure 3B)**. Such motions are completely absent from *Geo*HNH, thus two neighboring domains, *Geo*Rec2 and *Geo*HNH, diverge in their intrinsic flexibility (at least in isolation), raising questions about the functional implications of these motions in *Geo*Rec2. We previously showed that heightened flexibility of *Spy*Rec3 via specificity-enhancing mutations concomitantly narrowed the conformational space sampled by *Spy*HNH, highlighting a "motional trade-off" between the domains. Manipulation of the flexibility

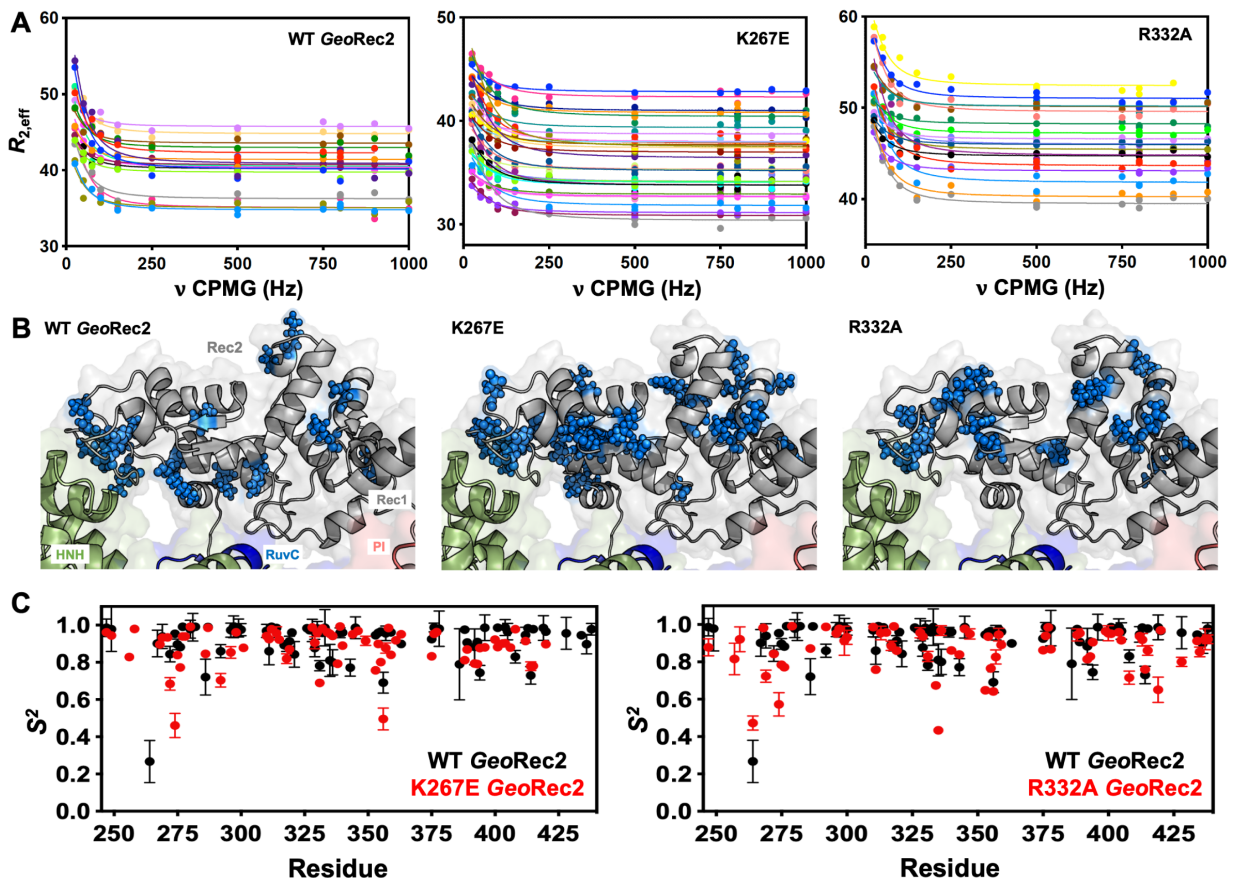

Figure 3. (A) CPMG relaxation dispersion profiles of all residues with evidence of µs-ms motion, fit to a global k_{ex} of 147 ± 41 s^{-1} (WT *Geo*Rec2, left), 376 ± 89 s^{-1} (K267E *Geo*Rec2, center), and 142 ± 28 s^{-1} (R332A *Geo*Rec2, right) collected at 25 °C and 600 MHz. Residues are colored in accordance with Table S1. Relaxation dispersion profiles for individual resonances are shown in Figures S8-S10. **(B)** Sites exhibiting CPMG relaxation dispersion in **(A)** are mapped to *Geo*Rec as blue spheres. Adjacent domains within the cryo-EM structure of *Geo*Cas9 are also shown. **(C)** Per-residue NMR order parameters of WT (black), K267E, and R332A (red, separate plots) *Geo*Rec.

193 of *Spy*Cas9 and *Geo*Cas9 domains by mutagenesis also impacts aspects of nucleic acid binding
194 and cleavage,[1,10,14,15,29] which led us to investigate similar perturbations in *Geo*Rec2.

195 Since *Spy*Rec3 and *Geo*Rec2 have similar structures and μs-ms flexibility, we speculated
196 that charge-altering mutations would modulate the biophysical properties of *Geo*Rec and the
197 function of *Geo*Cas9, as observed for *Spy*Cas9. We investigated K267E and R332A *Geo*Rec2 with
198 NMR spin relaxation, as described for WT *Geo*Rec2 (*vide supra*). An analysis of chemical
199 exchange rates, k_{ex}, derived from dual-field CPMG relaxation dispersion show a global k_{ex} for WT
200 *Geo*Rec2 of 147 ± 41 s^{-1}. The K267E mutation, which directly contacts the nucleic acids, shifts the
201 globally fitted k_{ex} to 376 ± 89 s^{-1}, while the R332A variant maintains a global k_{ex} similar to that of
202 WT *Geo*Rec2 (142 ± 28 s^{-1}) and consistent with its similar thermal stability. The global fit of the
203 K267E variant is based on CPMG profiles of 33 residues, while that of R332A is derived from 18
204 residues (**Table S1**). Interestingly, the residues participating in the global motions of both variants
205 are distinct from those of WT *Geo*Rec2, demonstrating that residue-specific flexibility is
206 redistributed throughout *Geo*Rec2, which suggests an altered intradomain molecular crosstalk
207 within the larger *Geo*Rec. Indeed, perturbation to NMR-detectable motions in *Spy*Cas9 rewired its
208 allosteric signaling and enzymatic function.[16,29] A similar dynamic modulation of *Geo*Cas9 may
209 fine-tune its DNA cleavage, which has been demonstrated within the *Geo*HNH nuclease[1] and
210 wedge (WED) domains.[32] We also assessed the ps-ns fluctuations of *Geo*Rec2 variants (a
211 negligible contribution to the WT *Geo*Rec2 dynamic profile) and calculated order parameters from
212 R_1, R_2 and ^{1}H-[^{15}N] NOE relaxation measurements (**Figure 3C**). Bond vector fluctuations on the
213 ps-ns timescale are only locally altered, thus the mutation-induced reshuffling of these motions is
214 negligible ($\langle \Delta S^2 \rangle \leq 0.1$) and suggests that, like WT *Geo*Rec2, ps-ns motion arises primarily from
215 global tumbling in solution.

216 ***Mutations within GeoRec alter its affinity for RNA***

217 The role of the Rec lobe in orienting the RNA:DNA hybrid within Cas9 is crucial to its
218 function.[10-13] Thus, the structure, motions, and nucleic acid interactions of Rec represent a critical
219 piece of the Cas9 signaling machinery. Previous studies of *Spy*Cas9 revealed that gRNA binding
220 to the Rec lobe induces a global structural rearrangement of the protein that positions the adjacent
221 HNH into its "proofreading" state,[15] after which target DNA binding positions the nucleases into
222 active conformations for cleavage.[15,34] We wondered if the atomistic details of the apo *Geo*Cas9-
223 to-RNP transition could be captured by NMR using the *Geo*Rec construct. In our previous studies,
224 we used an *in vitro* DNA cleavage assay with *Geo*Cas9 and a 141nt gRNA containing a 21nt spacer
225 targeting the mouse *Tnnt2* gene locus.[1] Since this assay was already established, we utilized the
226 same gRNA sequence. However, truncating this gRNA was necessary to optimize binding studies
227 for NMR analysis. We focused on the 5' end of the gRNA, which includes the spacer sequence,
228 based on the *Geo*Cas9 AlphaFold2 model and structural data from *Nme*Cas9 and *Spy*Cas9 showing
229 interactions between the Rec lobe and this region of the gRNA. The subsequent cryo-EM structure
230 of *Geo*Cas9 corroborated this interaction.[20] Initial attempts using a truncated 101nt portion of the
231 full gRNA resulted in poor NMR spectra. An overlay of the ^{1}H-^{15}N HSQC NMR spectra of apo
232 *Geo*Rec and *Geo*Rec-RNP at a 1:1 molar ratio showed extensive line broadening (**Figure S11**),
233 likely due to the large size of the complex (75.5 kDa). To mitigate this issue, a 39nt RNA
234 containing the 21bp spacer sequence was selected for its ability to maintain the NMR signal while
235 being long enough to interact fully with the Rec lobe, as suggested by prior structures (**Figure**
236 **S12**). When bound to *Geo*Rec, this complex is 55.6 kDa and a ^{1}H-^{15}N NMR spectral overlay of
237 apo *Geo*Rec and the domain bound to 39nt RNA shows clear, resolved resonances with significant
238 chemical shift perturbations and line broadening (**Figure 4A/B, S11**). The strongest chemical shift

239 perturbations are localized to the *Geo*Rec2 subdomain that interfaces with the RNA:DNA hybrid
240 at the PAM distal end, where previous studies of specificity-enhancing variants of *Spy*Cas9 have
241 identified alterations in nucleic acid binding to *Spy*Rec3.[16] It is not known whether specific
242 residues at the PAM distal binding interface of *Geo*Rec2 play a similar role. Line broadening is
243 evident in both *Geo*Rec1 and *Geo*Rec2, primarily localized to the RNA:DNA hybrid interface
244 revealed in recent *Geo*Cas9 structures. Microscale thermophoresis (MST) experiments quantified
245 the affinity of *Geo*Rec for this RNA, producing a K_d = 3.3 ± 1.5 μM that is consistent with the
246 concentration-dependent NMR chemical shift perturbations (**Figure 5A**).

247 To understand how the K267E and R332A mutants impact RNA binding to *Geo*Rec, we
248 conducted RNA titration experiments via NMR and observed that chemical shift perturbations

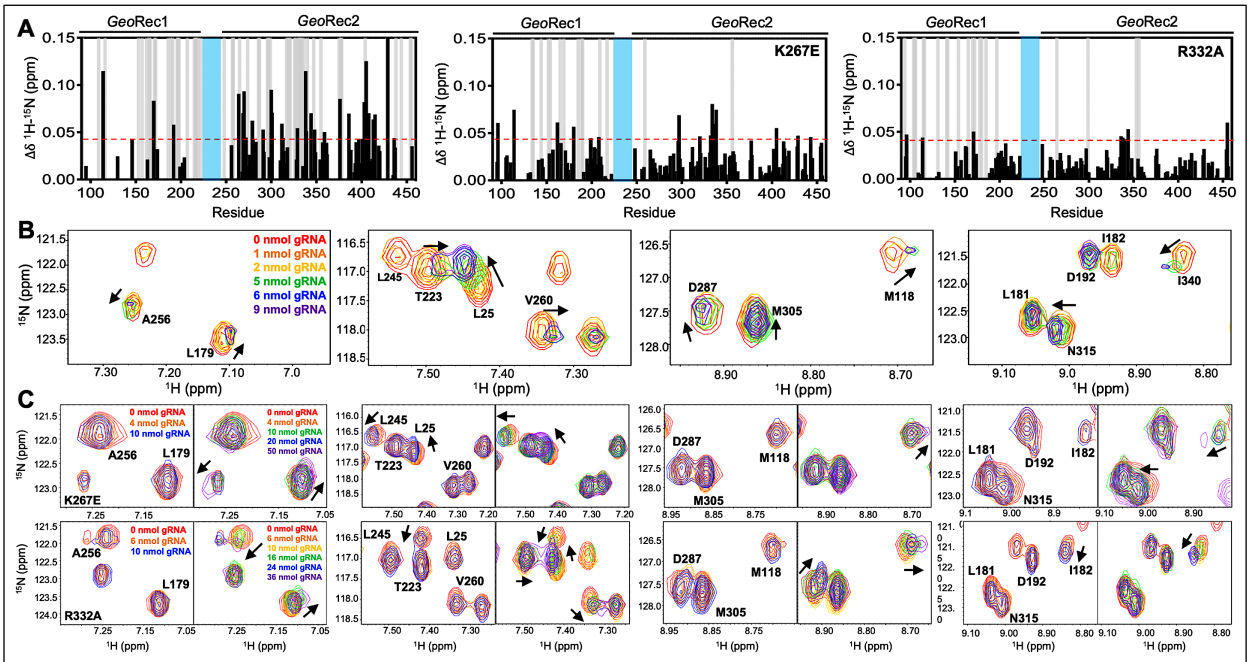

Figure 4. (A) NMR chemical shift perturbations caused by RNA binding to WT, K267E, and R332A *Geo*Rec. Gray bars denote sites of line broadening, and the blue bar denotes an unassigned region of *Geo*Rec corresponding to the flexible Rec1-Rec2 linker. The red dashed line indicates 1.5σ above the 10% trimmed mean of the data. **(B)** Representative NMR resonance shifts caused by titration of a 39nt portion of the full gRNA into WT *Geo*Rec. **(C)** NMR titration of 39nt RNA into K267E (top) and R332A (bottom) *Geo*Rec. The left panel of each pair demonstrates that minimal change in NMR chemical shift or resonance intensity is apparent at RNA concentrations mimicking the WT titration. The right panel of each pair depicts the titration over a three-fold wider concentration range of RNA, where shifts and line broadening are visible. Representative resonances are colored by increasing RNA concentration in the legend.

249 were attenuated in both variants, relative to WT *Geo*Rec. Despite this muted structural effect, the
250 impact from RNA-induced line broadening remains substantial in the *Geo*Rec1 subdomain. Our
251 NMR data revealed that a three-fold greater concentration of RNA was required to induce the
252 maximal structural and dynamic effects in the variants than is required for WT *Geo*Rec **(Figure**
253 **4A/C**), suggesting that the variants have a reduced RNA affinity. MST experiments showed
254 statistically significant reductions in RNA affinity for the K267E and R332A constructs, relative
255 to WT *Geo*Rec, where K267E *Geo*Rec produced a K_d = 7.2 ± 1.0 μM and R332A *Geo*Rec
256 produced a K_d = 7.2 ± 1.5 μM (**Figure 5B**). The ~2-fold increase in K_d may also be due, in part, to
257 a change in the binding mode of the RNA, such as a faster k_{off}. Collectively, these data reveal that
258 mutations within *Geo*Rec primarily alter its structure around the mutation site with weaker distal
259 effects, but more significantly impact protein dynamics and in turn, the RNA interaction. NMR
260 experiments also demonstrate that the presence of RNA impacts both subdomains of *Geo*Rec,
261 providing a significant structural interface for additional molecular tuning of nucleic acid binding.

262 To investigate the impact of RNA binding on *Geo*Rec2 in greater detail, we conducted

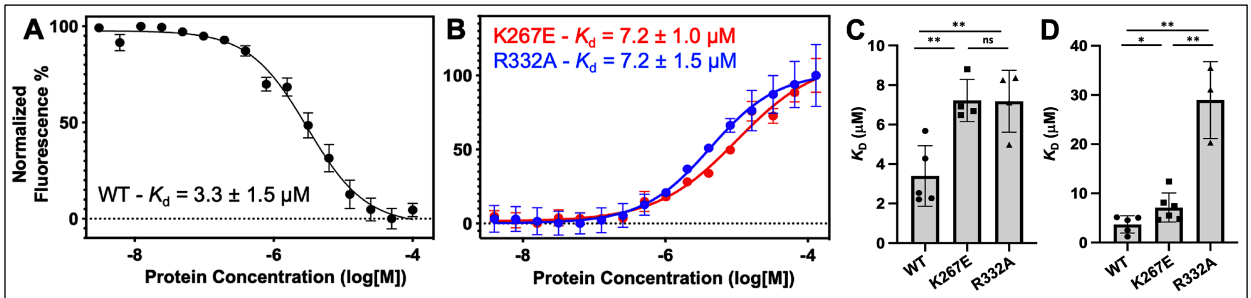

Figure 5. Representative MST-derived profiles of WT **(A)**, K267E, and R332A **(B)** *Geo*Rec binding to a Cy5-labeled 39nt portion of a gRNA, yielding K_d = 3.3 ± 1.5 μM, K_d = 7.2 ± 1.0 μM and K_d = 7.2 ± 1.5 μM, respectively. Bar graphs comparing K_d values across n ≥ 3 replicate samples are shown for Tnnt2 RNA **(C)** and 8UZA RNA from a recent cryo-EM structure **(D)**. *p < 0.05, **p < 0.004

263 NMR titration experiments using the isolated domain, which yielded even clearer NMR spectra.
264 **Figure S13** shows NMR spectra of WT, K267E, and R332A *Geo*Rec2 overlaid with their
265 corresponding RNA-bound spectra (39nt Tnnt2 RNA). At protein:RNA molar ratios used for full-

266 length *Geo*Rec studies, the WT *Geo*Rec2 spectrum exhibited significant line broadening across
267 the *Geo*Rec2 sequence. Plots of NMR peak intensities (I_{bound}/I_{free}) show substantial resonance
268 intensity losses (**Figure S13**), with many residues likely in the intermediate exchange regime, in
269 addition to the assumed changes in rotational correlation of the domain. In comparison, spectra of
270 the RNA-bound K267E and R332A *Geo*Rec2 variants showed less pronounced signal decay at the
271 same levels of titrant, retaining nearly double the I_{bound}/I_{free} ratio across these spectra (**Figure S13**).
272 These data are consistent with the results of NMR experiments with the 43 kDa *Geo*Rec,
273 supporting the premise that *Geo*Rec2 mutations weaken its interaction with RNA. The less
274 crowded NMR spectrum of isolated *Geo*Rec2 facilitated the resolution of distinct structural
275 features that explain the impact of the mutations on RNA binding (**Figure S9**). For example,
276 residue I53 adopts a similar conformation in RNA-bound WT and K267E *Geo*Rec2 but assumes
277 a different structural state in R332A. Conversely, residue R25 populates a WT-like structure in
278 RNA-bound R332A *Geo*Rec2, unlike K267E. Additionally, two resonances are observed for
279 residue K71 in the RNA-bound R332A NMR spectrum, indicating real-time equilibration between
280 two structural states. This effect is unique to the R332A variant and underscores subtle structural
281 and dynamic changes to *Geo*Rec during RNA binding.

282 We further examined the NMR data to attempt to identify residues most critical for RNA
283 binding to *Geo*Rec. In an overlay of the WT and mutant RNA-induced chemical shift perturbations
284 ($\Delta\delta$, **Figure S14**), it became clear that the effect of RNA binding to *Geo*Rec variants was muted,
285 where even at saturating concentrations, the chemical shift perturbations across the K267E and
286 R332A *Geo*Rec2 sequences were weaker than those of same residues in WT *Geo*Rec. The residual
287 $\Delta\delta$ (WT - mutant) was plotted (**Figure S14**), where positive values indicate that residues in a
288 *Geo*Rec variant are weakly affected by RNA, relative to WT. Negative residual $\Delta\delta$ denote sites

289 where *Geo*Rec variants experience a greater structural impact from RNA than corresponding sites
290 in WT. Of particular interest are the positive residuals that hint at the sites in *Geo*Rec most critical
291 for tight RNA binding. These residues were mapped onto the *Geo*Rec structure (**Figure S14**) and
292 termed allosteric hotspots, as many are not at the RNA interface. Mutations of these hotspots in
293 future studies offers a potential means of precisely tuning the affinity of *Geo*Rec to its gRNA.
294 Notably, residues with positive residual Δδ (suggested as critical for tight RNA binding) largely
295 overlap in the analysis of both variants. Specifically, residues F170, R192, H264, R269, L270,
296 L279, H300, D301, E368, D376, D403, E405, E408, and I429 appear as allosteric hotspots (with
297 CPMG relaxation dispersion) critical to WT-like RNA interaction.

298 Having observed a reduced affinity of *Geo*Rec variants for RNA by NMR and MST, we
299 next quantified the impact of the K267E and R332A mutations on RNP formation and stability in
300 full-length *Geo*Cas9. The thermal unfolding midpoint of full-length WT *Geo*Cas9 determined by
301 CD is ~60 °C and the K267E and R332A mutations do not change the T_m of the apo protein (**Figure**
302 **S15**). Upon formation of an RNP (using a full-length gRNA), the T_m of WT *Geo*Cas9 increases to
303 73°C. K267E *Geo*Cas9 retains a similar T_m increase to 70 °C, while R332A *Geo*Cas9 forms a less
304 stable RNP with T_m of 61 °C. The trend of these data is consistent with NMR and MST, which
305 highlight that although K267E and R332A mutations within *Geo*Rec have somewhat muted
306 structural effects, these changes alter protein dynamics and the interaction with gRNA.

307 ***Mutations in full-length GeoCas9 alter its structural dynamics and interaction with gRNA***

308 To further investigate the effects of mutations on protein dynamics, we performed
309 molecular dynamics (MD) simulations based on the cryo-EM structure of full-length *Geo*Cas9
310 (PDB: 8UZA) in complex with gRNA and target DNA. We simulated the full-length WT *Geo*Cas9
311 and its K267E and R332A mutants as well as a double mutant combining K267E and R332A

312 (**Figure 6A**), in three replicates of approximately 2 µs each. Multi-microsecond simulations

313 revealed substantial changes in the dynamics of the *Geo*Cas9 mutants compared to the WT (**Figure**

314 **S16**). Specifically, we observed that mutations in the REC domain significantly altered the

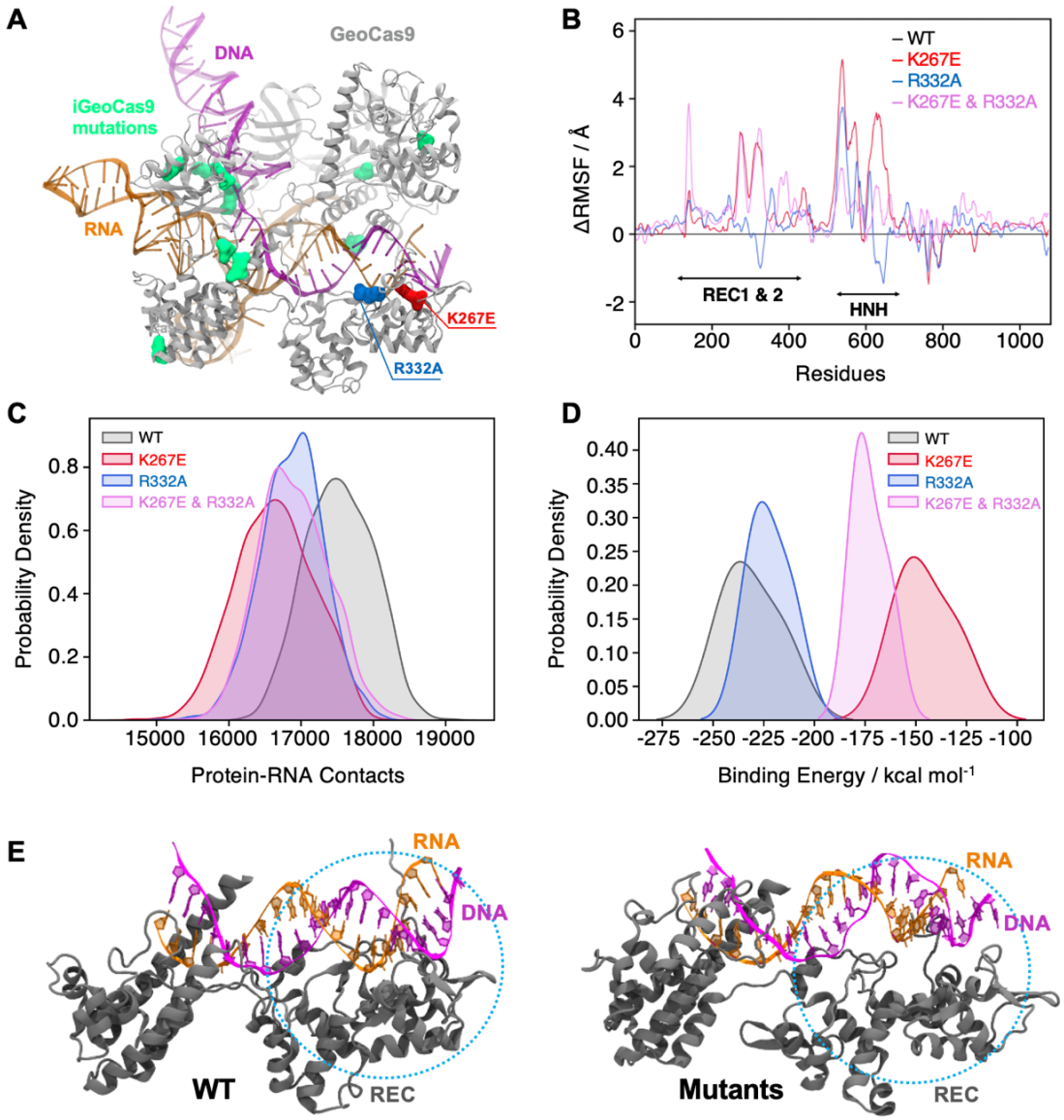

Figure 6: Effects of mutations in full-length *Geo*Cas9 revealed by MD simulations. **(A)** The structure of *Geo*Cas9 (PDB: 8UZA, protein in gray) bound to gRNA (orange) and DNA (magenta) is shown. Mutations studied include K267E (red), R332A (blue), and the 10 mutations of i*Geo*Cas9 (lime green), all highlighted in surface representation. **(B)** Differential root-mean-square fluctuations (ΔRMSF) of protein residues computed between WT *Geo*Cas9 and the K267E (red), R332A (blue), and double mutant (pink). **(C)** Distribution of protein-RNA contacts for WT and *Geo*Cas9 variants computed over the 6 µs simulation ensemble. **(D)** Comparison of gRNA binding free energy to the Rec domain in WT *Geo*Cas9 and variants. **(E)** Representative snapshots from MD simulations illustrating structural changes in Rec-gRNA association in WT *Geo*Cas9 (left) and variants (right).

315 dynamics of both the Rec and the adjacent HNH (**Figure S16**). Differential root-mean-square
316 fluctuations (ΔRMSF) analysis of protein residues between the WT and variants further
317 highlighted these alterations, showing increased dynamics in the HNH and Rec domains induced
318 by the mutations (**Figure 6B**). To quantify the impact of these mutations, we analyzed protein-
319 RNA interactions by calculating the number of contacts between *Geo*Cas9 and gRNA in the WT
320 and mutant systems. A contact was defined as a distance between two atoms of ≤ 4.5 Å. The
321 number of contacts was significantly reduced in all variants compared to the WT, with the most
322 pronounced reduction observed in the K267E variant (**Figure 6C**). We next quantified gRNA-Rec
323 domain binding by calculating the binding free energy using the MM-GBSA method over ~200 ns
324 of stable simulation trajectories (details in Materials and Methods). Consistent with a reduction in
325 gRNA contacts, variants with the K267E mutation exhibited a substantial reduction in binding free
326 energy (>60 kcal mol^{-1}) relative to the WT, whereas the R332A variant displayed a smaller
327 reduction (<20 kcal mol^{-1}, **Figure 6D**). Notably, protein-DNA interactions remained largely
328 unaffected, suggesting that these mutations do not impair *Geo*Cas9 DNA cleavage ability.

329 Additionally, we simulated a novel variant, i*Geo*Cas9 (PDB: 8UZB), containing mutations
330 in the Rec1 and WED domains (**Figure 6A**, mutations highlighted in lime green). This variant was
331 recently demonstrated to have enhanced specificity in genome-editing.[21] Intriguingly, i*Geo*Cas9
332 exhibited increased dynamics in the HNH and Rec domains, along with a reduction in gRNA
333 binding free energy similar to the K267E and R332A mutants. These results suggest a distinct
334 allosteric pathway involving additional residues that enables i*Geo*Cas9 to maintain improved DNA
335 cleavage activity despite reduced gRNA binding affinity. In fact, i*Geo*Cas9 samples the greatest
336 conformational space of any variant tested (**Figure S16**), suggesting a high level of flexibility is
337 critical to enhanced specificity in *Geo*Cas9. Collectively, our simulations reveal that mutations

338 K267E and R332A destabilize the *Geo*Cas9 interaction with gRNA, consistent with NMR
339 observations. Furthermore, the enhanced dynamics and altered binding affinities observed in
340 i*Geo*Cas9 indicate potential allosteric mechanisms that optimize its genome-editing functionality,
341 where K267E and R332A evoke a similar, but lesser degree of biophysical change.

342 ***DNA cleavage assays suggest the highly stable GeoCas9 is resistant to functional changes by***
343 ***K267E or R332A mutations***

344 The dynamic impact of the *Geo*Rec mutations and their altered gRNA interactions at the
345 biophysical level led us to speculate that either mutation incorporated into full-length *Geo*Cas9
346 would also alter its DNA cleavage function, especially at elevated temperatures where WT
347 *Geo*Cas9 is most active. Temperature-dependent functional alterations were previously observed
348 for single-point mutations within *Geo*HNH.[1] Although the K267E and R332A mutations slightly
349 diminished on-target DNA cleavage by *Geo*Cas9, the effect was very subtle and these overall
350 cleavage activities followed the temperature dependence of WT *Geo*Cas9 quite closely (**Figure**
351 **S17**).

352 To assess the impact of the K267E and R332A mutations on *Geo*Cas9 specificity, we
353 assayed the propensity for off-target cleavage using DNA substrates with mismatches 5-6 or 19-
354 20 base pairs from the PAM site (**Figure S18, Table S2**). As a control for on- and off-target
355 activity, we assayed WT *Spy*Cas9 alongside the widely used high-specificity HiFi-*Spy*Cas9
356 variant[24] (**Figure S18, Table S3**) and found a lower percent of digested off-target (mismatched)
357 DNA sequences when compared to WT *Spy*Cas9. As expected, WT *Geo*Cas9 was increasingly
358 sensitive to mismatched target sequences closer to the seed site, which has been demonstrated with
359 *Spy*Cas9 and other Cas systems.[2,6,8,35] No significant differences in activity were observed with
360 digestion durations ranging from 1-60 minutes,[2] implying that a 1-minute digestion is sufficient

361 for *in vitro* activity of *Geo*Cas9 with the target DNA template. While these findings generally align
362 with prior investigations of off-target DNA cleavage,[2,6,8] there are nuanced differences.
363 Specifically, a previous study reported ~10% cleavage of off-target DNA with a mismatch 5-6
364 base pairs from the PAM by WT *Geo*Cas9.[2] Our results showed nearly 50% cleavage for the same
365 off-target mismatch, but still a significant decrease in cleavage from on-target or 19-20 base pair
366 distal mismatches. This could be due to the relatively high RNP concentrations (600-900 nM) in
367 our assay (for clear visibility on the gel), compared to prior studies with RNP concentrations ≤ 500
368 nM.[2] Our results corresponded closely to those of prior studies with a 19-20 base pair mismatch,
369 where off-target cleavage is tolerated by WT *Geo*Cas9.[2] Single-point mutants K267E and R332A
370 *Geo*Cas9 have negligible impact on *Geo*Cas9 specificity (both variants follow the trend of WT
371 *Geo*Cas9, **Figure S18**), which contrasts prior work with *Spy*Cas9 that demonstrated robust
372 specificity enhancement with single-point mutations in Rec.[24,27] Additionally, a *Geo*Cas9 double
373 mutant K267E/R332A exhibits decreased on-target cleavage efficiency, which has been noted in
374 high-specificity Cas systems.[15,23,24,27,36-38] However, the additive effect of the K267E/R332A
375 double mutant still does not enhance *Geo*Cas9 specificity in our assay.

376 MST-derived binding affinities using full-length Tnnt2 gRNA and full-length WT, K267E,
377 or R332A *Geo*Cas9 indicate that all three proteins have similar affinities for the gRNA used in the
378 functional assays (**Figure 7**). Thus, mutations do not substantially alter full-length *Geo*Cas9
379 binding to Tnnt2 gRNA, supporting similar cleavage activities for these proteins. We repeated the
380 MST experiments using a different gRNA sequence derived from the new cryo-EM structure of
381 *Geo*Cas9 (PDB:8UZA), which has a different spacer sequence. We observed a similar trend, as all
382 *Geo*Cas9 variants exhibited comparable affinities for this gRNA. Our functional studies illustrate

383 an apparent resilience of *Geo*Cas9 to major functional changes at the level of Rec, despite

384 comparable mutations having profound functional impacts in mesophilic Cas9s.

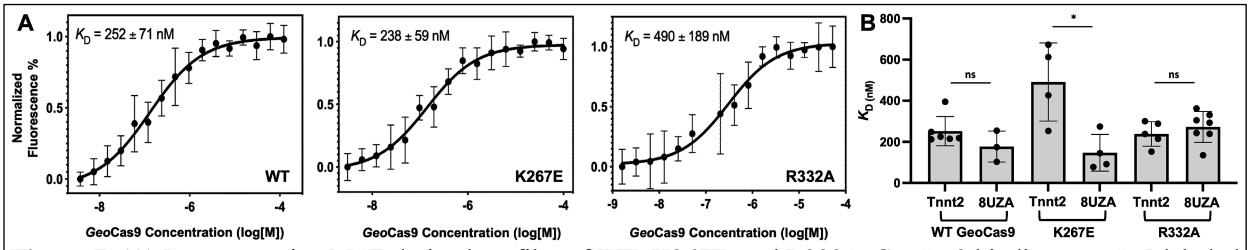

Figure 7. (A) Representative MST-derived profiles of WT, K267E, and R332A *Geo*Cas9 binding to a Cy5-labeled full-length Tnnt2 gRNA. **(B)** Bar graph comparing K_d values across n ≥ 3 replicate samples are shown for Tnnt2 and 8UZA gRNA from a recent cryo-EM structure of *Geo*Cas9. *$p < 0.01$

385 **Discussion**

386 CRISPR-Cas9 is a powerful tool for targeted genome editing with high efficiency and

387 modular specificity.[2,15,24,27] Allosteric signals propagate DNA binding information to the HNH and

388 RuvC nuclease domains, facilitating their concerted cleavage of double-stranded DNA.[8,10,14,15] The

389 intrinsic flexibility of the nucleic acid recognition lobe plays a critical role in this information

390 transfer, exerting a measure of conformational control over catalysis.[10] This study provides new

391 insights into the structural, dynamic, and functional role of the thermophilic *Geo*Cas9 recognition

392 lobe. Novel constructs of subdomains *Geo*Rec1 and *Geo*Rec2, as well as intact *Geo*Rec show a

393 high structural similarity to the domains in full-length *Geo*Cas9, facilitating solution NMR

394 experiments that captured the intrinsic allosteric motions across *Geo*Rec2. These studies revealed

395 the existence of μs-ms timescale motions that are classically associated with allosteric signaling

396 and enzyme function, which span the entire *Geo*Rec2 domain to its interfaces with *Geo*Rec1 and

397 the adjacent *Geo*HNH domain.

398 Based on homology to specificity-enhancing variants of the better studied *Spy*Cas9, the

399 biophysical and biochemical consequences of two mutations were tested in *Geo*Rec2, the larger

400 *Geo*Rec lobe, and full-length *Geo*Cas9. We speculated that removing positively charged residues

401 with potential to interact with negatively charged nucleic acids could disrupt *Geo*Cas9-gRNA

402 complex formation, stability, and subsequent function by altering the protein or nucleic acid
403 motions. Indeed, CPMG relaxation dispersion experiments revealed that mutations enhanced and
404 reorganized the μs-ms flexibility of *Geo*Rec2. Further, NMR titrations showed the affinity of
405 K267E and R332A *Geo*Rec for 39nt portions of two gRNAs to be weaker than that of WT *Geo*Rec,
406 consistent with MST-derived K_d values using the isolated domain. The mutations also diminished
407 the stability of the full-length *Geo*Cas9 RNP complex, though this could result from an allosteric
408 effect that destabilizes the *Geo*Cas9 structure without appreciably altering gRNA binding.

409 The collective changes to protein dynamics, gRNA binding, and RNP thermostability
410 suggested that mutations could modulate *Geo*Cas9 function, as observed in similar studies of
411 *Spy*Cas9 reporting that gRNA dynamics, affecting the potential for the RNA:DNA hybrid to
412 dissociate, have affected function.[11,15,39] Yet, the functional impact of single-point and double
413 mutations in this work were negligible, despite homologous K-to-E and R-to-A single point
414 mutations enhancing specificity of the mesophilic *Spy*Cas9. The biophysical impact of mutations
415 within *Geo*Rec2 and *Geo*Rec may be tempered by its evolutionary resilience and the highly stable
416 neighboring domains in the context of full-length *Geo*Cas9, reflected in an unchanged affinity for
417 target DNA once the RNP was formed.[40,41] Thus, a greater number of additive (or synergistic)
418 mutations within *Geo*Rec would be required to fine-tune activity or specificity to a large degree.

419 It should be noted that the effects of these and other *Geo*Rec mutations may vary *in vivo*
420 or with alternative target cleavage sites and cell types. Such studies will be the subject of future
421 work, as will biochemical assays of homologous mutations across diverse Cas9s, which have
422 contributed to the wide use of CRISPR technology.[42] We also note that despite the homology
423 between *Geo*Rec2 and *Spy*Rec3 and the latter's role in evo- and HiFi-*Spy*Cas9 variants that
424 inspired the K267E and R332A mutations, the maximally enhanced *Spy*Cas9 variants contain four

425 mutations each. Presumably each individual substitution plays a small role modulating specificity.
426 However, there is no consistent pattern that discerns whether multiple mutations will have additive
427 or synergistic impacts on Cas9 function. NMR and MD studies of high-specificity *Spy*Cas9
428 variants (HF-1, Hypa, and Evo, each with distinct mutations in the *Spy*Rec3 domain) reveal
429 universal structural and dynamic variations in regions of *Spy*Rec3 that interface with the
430 RNA;DNA hybrid.[16] Notably, a recently published variant, i*Geo*Cas9,[32] demonstrated enhanced
431 genome-editing capabilities in HEK293T cells with eight mutations, though none in the Rec2
432 subdomain. This study highlighted the functional adaptability of i*Geo*Cas9 under low magnesium
433 conditions, a trait beneficial in mammalian cells, distinguishing it from WT *Geo*Cas9. These very
434 recently published data, as well as the findings reported here still advance our molecular
435 understanding of the functional handles in *Geo*Cas9, relevant to the design of new enhanced
436 variants.

437 This study marks the first phase of mapping allosteric motions and pathways of information
438 flow in the *Geo*Rec lobe with solution NMR experiments. Such information transfer is critical to
439 the crosstalk between Rec and HNH in several Cas9s. Despite NMR advancements in
440 perdeuteration,[43] transverse relaxation-optimized spectroscopy (TROSY),[44] and sparse isotopic
441 labeling,[45] per-residue dynamics underlying allosteric signaling in large multi-domain proteins
442 such as *Geo*Cas9 (~126 kDa) have remained challenging to characterize. Novel cryo-EM
443 structures of *Geo*Cas9[32] will facilitate the merging of future NMR and MD simulation studies to
444 report on RNP dynamics and atomic level networks of communication. The identification of
445 additional (or synergistic) allosteric hotspots within *Geo*Rec using an integrated workflow will
446 help to further resolve the balance between structural flexibility and the unusually high stability of

447 *Geo*Cas9, leading to new insight into targeted manipulation of RNA affinity and enhanced
448 variants.

449 Here, we set out to biophysically characterize the Rec lobe of *Geo*Cas9 to obtain new
450 understanding of its function (in the context of well-studied mesophilic Cas9s). Using an
451 AlphaFold2 model, and later a cryo-EM structure of *Geo*Cas9, we introduced mutations based on
452 proximal gRNA interactions and homology to specificity-enhancing sites in *Spy*Cas9. However,
453 the mutations did not affect *Geo*Cas9 function as expected, highlighting the complicated interplay
454 between the biophysics of mesophilic and thermophilic Cas enzymes and the difficulty of applying
455 universal functional predictions to Cas9. The very recent report of the i*Geo*Cas9 variant further
456 reinforces this point.[21] While high-specificity *Spy*Cas9 variants are heavily mutated in Rec3
457 (analogous to *Geo*Rec2), i*Geo*Cas9 lacks mutations in Rec2 entirely, raising new questions about
458 the functional role of *Geo*Rec. MD simulations of WT *Geo*Cas9, i*Geo*Cas9, and the Rec variants
459 revealed that while K267E and R332A induce dynamic effects on a similar trajectory to i*Geo*Cas9,
460 a true high-specificity variant samples a very wide conformational space with displacements of
461 both Rec and HNH (**Figures 6** and **S16**). Through further study of the fundamental mechanism of
462 *Geo*Cas9, it remains possible that engineering of *Geo*Rec may produce high-specificity variants.

463 **Materials and Methods**

464 **Expression and purification of *Geo*Rec1, *Geo*Rec2, *Geo*Rec, and *Geo*Cas9**

465 The *Geo*Rec1 (residues 90-225) and *Geo*Rec2 (residues 245-456) subdomains, as well as
466 the entire *Geo*Rec lobe (residues 90-456) of *G. stearothermophilus* Cas9 were engineered into a
467 pET28a vector with a N-terminal His_6-tag and a TEV protease cleavage site. The K267E and
468 R332A mutations were separately introduced into the *Geo*Rec2 plasmid. Plasmids were
469 transformed into BL21 (DE3) cells (New England Biolabs). Protein samples for CD spectroscopy,

470 MST, and functional assays were grown in Lysogeny Broth (LB, Fisher), while isotopically
471 labeled samples for NMR were grown in M9 minimal media (deuterated for *Geo*Rec2 and
472 *Geo*Rec) containing $CaCl_2$, $MgSO_4$, MEM vitamins, and 1.0 g/L ^{15}N ammonium chloride
473 and 2.0 g/L ^{13}C glucose (Cambridge Isotope Laboratories), as the sole nitrogen and carbon sources,
474 respectively. Cells were induced with 1 mM IPTG after reaching an OD_{600} of 0.8−1.0 and grown
475 for 4 hours at 37 °C post induction. The cells were harvested by centrifugation, resuspended in a
476 buffer of 50 mM Tris-HCl, 250 mM NaCl, 5 mM imidazole, and 1 mM PMSF at pH 7.4, lysed by
477 ultrasonication, and purified by Ni−NTA affinity chromatography. Following TEV proteolysis of
478 the terminal His-tag, the samples were further purified on a Superdex75 size exclusion column.
479 NMR samples were dialyzed into a buffer containing 20 mM NaPi, 80mM KCl, 1mM DTT, and
480 1mM EDTA at pH 7.4.

481 The full-length *Geo*Cas9 plasmid was acquired from Addgene (#87700), expressed in TB
482 media and was expressed and purified as previously described.[2] The K267E, R332A, and
483 K267E/R332A variants were introduced into full-length *Geo*Cas9 by modifying the original
484 plasmid acquired from Addgene.

485 **NMR spectroscopy**

486 Backbone resonance assignments of *Geo*Rec1 and *Geo*Rec2 were carried out on a Bruker
487 Avance NEO 600 MHz spectrometer at 25 °C. The following triple resonance experiments were
488 collected for each sample: ^{1}H-^{15}N TROSY-HSQC, HNCA, HN(CO)CA, HN(CA)CB,
489 HN(COCA)CB, HN(CA)CO and HNCO. All spectra were processed in NMRPipe[46] and analyzed
490 in Sparky[47]. Three-dimensional correlations and assignments were made in CARA[48] and *Geo*Rec1
491 and *Geo*Rec2 backbone assignments were deposited in the BMRB under accession numbers 52363
492 and 51197, respectively. Backbone resonance assignments of *Geo*Rec were completed by

transferring assignments from the individually assigned spectra of *Geo*Rec1 and *Geo*Rec2, as done previously for other large Cas9 fragments.[49,50]

NMR spin relaxation experiments were carried out in a temperature-compensated manner at 600 and 850 MHz on Bruker Avance NEO and Avance III HD spectrometers, respectively. CPMG experiments were adapted from the report of Palmer and coworkers[51] with a constant relaxation period of 20 ms and ν_{CPMG} values of 0, 25, 50, 75, 100, 150, 250, 500, 750, 800, 900, and 1000 Hz. Exchange parameters were obtained from global fits of the data carried out with RELAX[52] using the R2eff, NoRex, and CR72 models, as well as in-house fitting in GraphPad Prism with the following models:

Model 1: No exchange

$$R_2^{eff} = R_2^0 \tag{1}$$

Model 2: Two-state, fast exchange (Meiboom equation [53])

$$R_2^{eff} = R_2^0 + \frac{\Phi}{k_{ex}}\left[1 - \frac{4\nu_{CPMG}}{k_{ex}} \tan h\left(\frac{k_{ex}}{4\nu_{CPMG}}\right)\right] \tag{2}$$

Global fitting of CPMG profiles was determined to be superior to individual fits based on the Akaike Information Criterion.[54] Uncertainties in these rates were determined from replicate spectra with duplicate relaxation delays of 0, 25, 50 (×2), 75, 100, 150, 250, 500 (×2), 750, 800 (×2), 900, and 1000 Hz.

Longitudinal and transverse relaxation rates were measured with randomized T_1 delays of 0, 20, 60, 100, 200, 600, 800, and 1200 ms and T_2 delays of 0, 16.9, 33.9, 50.9, 67.8, 84.8, and 101.8 ms. Peak intensities were quantified in Sparky and the resulting decay profiles were analyzed in Sparky with errors determined from the fitted parameters. Uncertainties in these rates were determined from replicate spectra with duplicate relaxation delays of 20 (x2), 60 (x2), 100, 200, 600 (x2), 800, and 1200 ms for T_1 and 16.9, 33.9 (x2), 50.9 (x2), 67.8 (x2), 84.8, 101.8 (x2) ms for T_2. Steady-state ^{1}H-[^{15}N] NOE were measured with a 6 second relaxation delay followed by a

519 3 second saturation (delay) for the saturated (unsaturated) experiments and calculated by I_{sat}/I_{ref}.
520 All relaxation experiments were carried out in a temperature-compensated interleaved manner.

521 Model-free analysis was carried out by fitting relaxation rates to five different forms of the
522 spectral density function with local τ_m, spherical, prolate spheroid, oblate spheroid, or ellipsoid
523 diffusion tensors.[55-60] The criteria for inclusion of resonances in the diffusion tensor estimate was
524 based on the method of Bax and coworkers.[61] N-H bond lengths were assumed to be 1.02 Å and
525 the ^{15}N chemical shift anisotropy tensor was -160 ppm. Diffusion tensor parameters were
526 optimized simultaneously in RELAX under the full automated protocol.[52] Model selection was
527 iterated until tensor and order parameters did not deviate from the prior iteration.

528 NMR titrations were performed on a Bruker Avance NEO 600 MHz spectrometer at 25 °C
529 by collecting a series of ^{1}H-^{15}N TROSY HSQC spectra with increasing ligand (*i.e.* RNA)
530 concentration. The ^{1}H and ^{15}N carrier frequencies were set to the water resonance and 120 ppm,
531 respectively. Samples of WT, K267E, and R332A *Geo*Rec were titrated with a 39nt portion of a
532 gRNA until no further spectral perturbations were detected. NMR chemical shift perturbations
533 were calculated as:

534 $$\Delta\delta = \sqrt{(\Delta\delta_{HN}^2 + \Delta\delta_{NH}^2/25)/2}$$

535 **Microscale thermophoresis (MST)**

536 MST experiments were performed on a Monolith X instrument (NanoTemper
537 Technologies), quantifying WT, K267E, R332A, and K267E/R332A *Geo*Rec binding to a 39-nt
538 Cy5-labeled RNA at a concentration of 20 nM in a buffer containing 20 mM sodium phosphate,
539 150 mM KCl, 5 mM $MgCl_2$, and 0.1% Triton X-100 at pH 7.6. The *Geo*Rec proteins were serially
540 diluted from a 200 μM stock into 16 microcentrifuge tubes and combined in a 1:1 molar ratio with
541 serially diluted gRNA from a 40 nM stock. After incubation for 5 minutes at 37 °C in the dark,

542 each sample was loaded into a capillary for measurement. K_d values for the various complexes
543 were calculated using the MO Control software (NanoTemper Technologies). Statistical
544 significance was calculated using a two-tailed T-test.

545 **Circular dichroism (CD) spectroscopy**

546 All *Geo*Cas9 and *Geo*Rec proteins were buffer exchanged into a 20 mM sodium phosphate
547 buffer at pH 7.5, diluted to 1 μM, and loaded into a 2 mm quartz cuvette (JASCO instruments). A
548 CD spectrum was first measured between 200 - 250 nm, after which the sample was progressively
549 heated from 20 – 90 °C in 1.0 °C increments while ellipticity was monitored at 222 and 208 nm.
550 Phosphate buffer baseline spectra were subtracted from the sample measurements. Prior to CD
551 measurements, *Geo*Cas9-RNP was formed by incubating 3 μM *Geo*Cas9 with its gRNA at a 1:1.5
552 molar ratio at 37 °C for 10 minutes. The unfolding CD data was fit in GraphPad Prism to:

553 $$Ellipticity\ (T) = \frac{[(m_f T + b_f) + (m_u T + b_u)]\, exp\left[\left(-\frac{\Delta H_{D,vH}}{R}\right)\left(\frac{1}{T} - \frac{1}{T_m}\right)\right]}{1 + exp\left[\left(-\frac{\Delta H_{D,vH}}{R}\right)\left(\frac{1}{T} - \frac{1}{T_m}\right)\right]}$$

554 **X-ray crystallography**

555 *Geo*Rec protein purified as described above was crystallized by sitting drop vapor diffusion
556 at room temperature by mixing 1.0 μL of 15 mg/mL *Geo*Rec in a buffer of 20 mM HEPES and
557 100 mM KCl at pH 7.5 with 2.0 μL of crystallizing condition: 0.15 M calcium chloride, 15 %
558 polyethylene glycol 6000, 0.1 M HEPES at pH 7.0. Crystals were cryoprotected in crystallizing
559 condition supplemented with 30% ethylene glycol. Diffraction images were collected at the NSLS-
560 II AMX beamline at Brookhaven National Laboratory under cryogenic conditions. Images were
561 processed using XDS[62] and Aimless in CCP4.[63] Chain A of the *N. meningitidis* Cas9 X-ray
562 structure (residues 249-445 only, PDB ID: 6JDQ) was used for molecular replacement with Phaser
563 followed by AutoBuild in Phenix.[64] Electron density was only observed for the *Geo*Rec2

564 subdomain. The *Geo*Rec2 structure was finalized through manual building in Coot[65] and
565 refinement in Phenix.

566 **Molecular dynamics (MD) simulations**

567 Molecular Dynamics (MD) simulations were based on the cryo-EM structure of full-length
568 *Geo*Cas9 (PDB: 8UZA, resolution 3.17 Å) in complex with gRNA and target DNA with two
569 mutations in *Geo*Cas9 (at residues 8 and 582). Four systems were considered for the MD studies:
570 WT, K267E, R332A, K267E/R332A and i*Geo*Cas9. We generated the WT *Geo*Cas9 by back-
571 mutating A8D and A582H from the cryo-EM structure (PDB: 8UZA), followed by introducing the
572 mutations K267E, R332A, or a double mutation (with both K267E and R332A) for the variant
573 systems. Subsequently, we performed MD simulation of i*Geo*Cas9 (PDB: 8UZB, resolution 2.63
574 Å) consisting of 10 mutations (D8A, E149G, T182I, N206D, P466Q, H582A, Q817R, E843K,
575 E854G, K908R). All systems were solvated with explicit water in a periodic box of ~ 134 Å x ~
576 154 Å x ~ 151 Å resulting in ~ 276,000 atoms. Counter ions were added to neutralize the systems.
577 MD simulations were performed using a protocol tailored for protein-nucleic acid complexes,[66]
578 previously applied in studies of CRISPR-Cas systems.[67-69] All the simulations were performed by
579 using Amber ff19SB force field for protein,[70] ff99bsc1 corrections and χOL3 corrections for DNA
580 and RNA, respectively.[71,72] Water molecules were described by TIP3P model.[73] All bonds
581 involving hydrogens were constrained using the LINCS algorithm. A particle mesh Ewald method
582 (PME) with a 10 Å cutoff was used to calculate electrostatics. Energy minimization was performed
583 to relax the water molecules and counterions, keeping the protein-nucleic acid complex fixed with
584 harmonic potential restraints of 100 kcal/mol $Å^2$. Equilibration was performed by gradually
585 increasing the temperature from 0 to 100 K and then to 200 K in canonical NVT ensemble and
586 isothermal-isobaric NPT ensemble. A final temperature of 300 K was maintained via Langevin

587 dynamics with a collision frequency γ = 1/ps and a reference pressure of 1 atm was achieved
588 through Berendsen barostat. Production runs were carried out in NVT ensemble for 2 μs for each
589 system in three replicates, resulting in 6 μs per system (totaling 30 μs for all systems). The
590 equations of motion were integrated with the leapfrog Verlet algorithm with a time step of 2 fs.
591 All simulations were conducted using the GPU-empowered version of AMBER 22.[74] Analysis was
592 performed on the aggregate ensemble (i.e., ~6 μs per system).

593 To characterize the protein-nucleic acid interactions in all the systems under investigation,
594 we performed contact analysis. A contact was considered to form between two atoms within a
595 cutoff distance of ≤4.5 Å. The binding free energy of gRNA and DNA with *Geo*Cas9 was
596 calculated using the Molecular Mechanics Generalized Born Surface Area (MM-GBSA)
597 method.[75-77] This approach was used to compare the Rec-gRNA binding affinity of WT *Geo*Cas9
598 with its mutants. For each system, the binding energies were calculated over the ~200 ns ensemble
599 of the stable trajectories at an interval of ~20 ns.

600 **DNA cleavage assays**

601 *Geo*Cas9 gRNA templates containing 21-nt spacers targeting the mouse *Tnnt2* gene locus
602 were introduced into EcoRI and BamHI sites in pUC57 (Genscript). The plasmid was transformed
603 into BL21(DE3) cells (New England BioLabs) and subsequent restriction digest of the plasmid
604 DNA was carried out using the BamHI restriction enzyme (New England BioLabs) according to
605 the manufacturer's instructions. Linearized plasmid DNA was immediately purified using the
606 DNA Clean and Concentrator-5 kit (Zymo Research) according to the manufacturer's instructions.
607 RNA transcription was performed *in vitro* with the HiScribe T7 High Yield RNA Synthesis Kit
608 (New England BioLabs). DNA substrates containing the target cleavage site (479 base pairs,
609 **Figure S13**) were produced by polymerase chain reaction (PCR) using mouse genomic DNA as a

610 template and primer pairs 5'CAAAGAGCTCCTCGTCCAGT3' and 5'
611 ATGGACTCCAGGACCCAAGA3' followed by a column purification using the NucleoSpin®
612 Gel and PCR Clean-up Kit (Macherey-Nagel). For the *in vitro* activity assay, RNP formation was
613 achieved by incubating 3 μM *Geo*Cas9 (WT, K267E, R332A, or K267E/R332A mutant) and 3
614 μM gRNA at either 37 °C, 60 °C, 75 °C, or 85 °C for 30 minutes in a reaction buffer of 20 mM
615 Tris, 100 mM KCl, 5 mM $MgCl_2$, 1 mM DTT, and 5% glycerol at pH 7.5. The 10 μL cleavage
616 reactions were set up by mixing RNP at varying concentrations with 149 nanograms of PCR
617 products on ice followed by incubation at 37 °C for 30 minutes. The reaction was quenched with
618 1 μL of proteinase K (20 mg/mL) and subsequent incubation at 56 °C for 10 minutes. 6x DNA
619 loading buffer was added to each reaction and 10 μL of reaction mixture per lane was loaded onto
620 an agarose gel. DNA band intensity measurements were carried out with ImageJ.

621 For *in vitro* off-target activity assays, RNP formation was achieved by incubating 10 μM
622 *Geo*Cas9 (WT, K267E, R332A, or K267E/R332A mutant) and 10 μM gRNA at 37 °C for 30
623 minutes in the reaction buffer described above. The 10 μL cleavage reactions were set up by
624 mixing 1 μM RNP with 150 nanograms of PCR products (off-target DNA sequences listed in
625 **Table S2**) on ice followed by incubation at 37 °C for varying time points. The reaction was
626 quenched with 1 μL of proteinase K (20 mg/mL) and subsequent incubation at 56 °C for 10
627 minutes. 6x DNA loading buffer was added to each reaction and 10 μL of reaction mixture per
628 lane was loaded onto an agarose gel. DNA band intensity measurements were carried out with
629 ImageJ. WT and HiFi *Spy*Cas9 control proteins were purchased from Integrated DNA
630 Technologies (IDT, cat. No. 108158 and No. 108160, respectively), as was the associated *Spy*Cas9
631 gRNA, Alt-R™ CRISPR-Cas9 gRNA, with an RNA spacer sequence complementing 5'-

632 TGGACAGAGCCTTCTTCTTC-3'. The on-target and off-target DNA sequences used for the
633 *Spy*Cas9 *in vitro* cleavage assay can be found in **Table S3**.

634 **Author Contributions**

635 **HBB** and **ALK** produced *Geo*Rec2, *Geo*Rec1, *Geo*Rec, and *Geo*Cas9 proteins and RNAs,
636 conducted the NMR and biophysical experiments, analyzed the data, and wrote the original draft
637 of the manuscript. **AMD** solved the X-ray crystal structure of *Geo*Rec2. **CP** carried out MD
638 simulations and analyzed the data. **ZF** and **JL** conducted *Geo*Cas9 functional assays and analyzed
639 the data. **GP** supervised the MD studies and obtained funding. **GJ** supervised collection of X-ray
640 crystallographic data. **GPL** conceived the study, supervised collection of NMR spectroscopic data,
641 obtained funding, and wrote the original draft. The final manuscript was written and edited with
642 contributions from all authors.

643 **Acknowledgments**

644 This work was supported by NIH grant R01 GM 136815 (to GP and GPL) and NSF grant
645 MCB 2143760 (to GPL). GP acknowledges support from the NIH (Grant No. R01GM141329) and
646 the NSF (CHE- 2144823), as well as from the Sloan Foundation (FG-2023-20431) and the Camille
647 and Henry Dreyfus Foundation (TC-24-063). This research used the AMX beamline of the
648 National Synchrotron Light Source II, a U.S. Department of Energy (DOE) Office of Science User
649 Facility operated for the DOE Office of Science by Brookhaven National Laboratory under
650 Contract No. DE-SC0012704. The Center for BioMolecular Structure (CBMS) is primarily
651 supported by NIGMS through a Center Core P30 Grant (P30 GM133893), and by the DOE Office
652 of Biological and Environmental Research (KP1607011). Computational studies were carried out
653 using Expanse at the San Diego Supercomputing Center through allocation MCB160059 and
654 Bridges2 at the Pittsburgh Supercomputer Center through allocation BIO230007 from the

Advanced Cyberinfrastructure Coordination Ecosystem: Services & Support (ACCESS) program, which is supported by NSF grants #2138259, #2138286, #2138307, #2137603, and #2138296.

References

1 Belato, H. B. *et al.* Disruption of electrostatic contacts in the HNH nuclease from a thermophilic Cas9 rewires allosteric motions and enhances high-temperature DNA cleavage. *The Journal of Chemical Physics* **157**, 225103, doi:10.1063/5.0128815 (2022).

2 Harrington, L. B. *et al.* A thermostable Cas9 with increased lifetime in human plasma. *Nat Commun* **8**, 1424, doi:10.1038/s41467-017-01408-4 (2017).

3 Zhang, S. *et al.* Current Trends of Clinical Trials Involving CRISPR/Cas Systems. *Front. Med.* **10**, DOI: 10.3389/fmed.2023.1292452 (2023).

4 Li, T. *et al.* CRISPR/Cas Therapeutics: Progress and Prospects. *Signal Trans. Targ. Ther.* **8**, DOI: 10.1038/s41392-41023-01309-41397 (2023).

5 Kim, E. *et al.* In vivo genome editing with a small Cas9 orthologue derived from Campylobacter jejuni. *Nat Commun* **8**, 14500, doi:10.1038/ncomms14500 (2017).

6 Lee, C. M., Cradick, T. J. & Bao, G. The Neisseria meningitidis CRISPR-Cas9 System Enables Specific Genome Editing in Mammalian Cells. *Mol Ther* **24**, 645-654, doi:10.1038/mt.2016.8 (2016).

7 Belato, H. B. *et al.* Structural and dynamic insights into the HNH nuclease of divergent Cas9 species. *J Struct Biol* **214**, 107814, doi:10.1016/j.jsb.2021.107814 (2021).

8 Jinek, M. *et al.* A programmable dual-RNA-guided DNA endonuclease in adaptive bacterial immunity. *Science* **337**, 816-821, doi:10.1126/science.1225829 (2012).

9 Eggers, A. R. *et al.* Rapid DNA unwinding accelerates genome editing by engineered CRISPR-Cas9. *Cell* **187**, 3249-3261.e3214, doi:10.1016/j.cell.2024.04.031 (2024).

10 Palermo, G. *et al.* Key role of the REC lobe during CRISPR-Cas9 activation by 'sensing', 'regulating', and 'locking' the catalytic HNH domain. *Q Rev Biophys* **51**, doi:10.1017/s0033583518000070 (2018).

11 Dagdas, Y. S., Chen, J. S., Sternberg, S. H., Doudna, J. A. & Yildiz, A. A conformational checkpoint between DNA binding and cleavage by CRISPR-Cas9. *Sci Adv* **3**, eaao0027, doi:10.1126/sciadv.aao0027 (2017).

12 Mir, A., Edraki, A., Lee, J. & Sontheimer, E. J. Type II-C CRISPR-Cas9 Biology, Mechanism, and Application. *ACS Chem Biol* **13**, 357-365, doi:10.1021/acschembio.7b00855 (2018).

13 Jiang, F., Zhou, K., Ma, L., Gressel, S. & Doudna, J. A. STRUCTURAL BIOLOGY. A Cas9-guide RNA complex preorganized for target DNA recognition. *Science* **348**, 1477-1481, doi:10.1126/science.aab1452 (2015).

14 Sternberg, S. H., LaFrance, B., Kaplan, M. & Doudna, J. A. Conformational control of DNA target cleavage by CRISPR-Cas9. *Nature* **527**, 110-113, doi:10.1038/nature15544 (2015).
15 Chen, J. S. *et al.* Enhanced proofreading governs CRISPR-Cas9 targeting accuracy. *Nature* **550**, 407-410, doi:10.1038/nature24268 (2017).
16 Skeens, E. *et al.* High-fidelity, hyper-accurate, and evolved mutants rewire atomic-level communication in CRISPR-Cas9. *Sci Adv* **10**, eadl1045, doi:10.1126/sciadv.adl1045 (2024).
17 East, K. W. *et al.* Allosteric Motions of the CRISPR-Cas9 HNH Nuclease Probed by NMR and Molecular Dynamics. *Journal of the American Chemical Society*, doi:10.1021/jacs.9b10521 (2020).
18 Palermo, G., Miao, Y., Walker, R. C., Jinek, M. & McCammon, J. A. Striking Plasticity of CRISPR-Cas9 and Key Role of Non-target DNA, as Revealed by Molecular Simulations. *ACS Cent Sci* **2**, 756-763, doi:10.1021/acscentsci.6b00218 (2016).
19 Wu, Z., Yang, H. & Colosi, P. Effect of genome size on AAV vector packaging. *Mol Ther* **18**, 80-86, doi:10.1038/mt.2009.255 (2010).
20 Shen, P. *et al.* Structure of *Geobacillus stearothermophilus* Cas9: Insights into the Catalytic Process and Thermostability of CRISPR-Cas9. *ACS Catalysis* **14**, 13227-13235 (2024).
21 Eggers, A. R. *et al.* Rapid DNA Unwinding Accelerates Genome Editing by Engineered CRISPR-Cas9. *Cell* **187**, 3249-3261 (2024).
22 Lisi, G. P., East, K. W., Batista, V. S. & Loria, J. P. Altering the allosteric pathway in IGPS suppresses millisecond motions and catalytic activity. *Proc Natl Acad Sci U S A* **114**, E3414-e3423, doi:10.1073/pnas.1700448114 (2017).
23 Slaymaker, I. M. *et al.* Rationally engineered Cas9 nucleases with improved specificity. *Science* **351**, 84-88, doi:10.1126/science.aad5227 (2016).
24 Vakulskas, C. A. *et al.* A high-fidelity Cas9 mutant delivered as a ribonucleoprotein complex enables efficient gene editing in human hematopoietic stem and progenitor cells. *Nat Med* **24**, 1216-1224, doi:10.1038/s41591-018-0137-0 (2018).
25 Guzman, I., Ghaemi, Z., Baranger, A., Luthey-Schulten, Z. & Gruebele, M. Native Conformational Dynamics of the Spliceosomal U1A Protein. *The Journal of Physical Chemistry B* **119**, 3651-3661, doi:10.1021/jp511760m (2015).
26 Doudna, J. A. & Charpentier, E. Genome editing. The new frontier of genome engineering with CRISPR-Cas9. *Science* **346**, 1258096, doi:10.1126/science.1258096 (2014).
27 Casini, A. *et al.* A highly specific SpCas9 variant is identified by in vivo screening in yeast. *Nat Biotechnol* **36**, 265-271, doi:10.1038/nbt.4066 (2018).
28 Ricci, C. G. *et al.* Deciphering Off-Target Effects in CRISPR-Cas9 through Accelerated Molecular Dynamics. *ACS Cent Sci* **5**, 651-662, doi:10.1021/acscentsci.9b00020 (2019).
29 Nierzwicki, L. *et al.* Enhanced specificity mutations perturb allosteric signaling in CRISPR-Cas9. *Elife* **10**, doi:10.7554/eLife.73601 (2021).
30 Nierzwicki, Ł. *et al.* Principles of target DNA cleavage and the role of Mg2+ in the catalysis of CRISPR–Cas9. *Nature Catalysis* **5**, 912-922, doi:10.1038/s41929-022-00848-6 (2022).

31 Shen, P. *et al.* Structure of Geobacillus stearothermophilus Cas9: Insights into the Catalytic Process and Thermostability of CRISPR-Cas9. *ACS Catalysis* **14**, 13227-13235, doi:10.1021/acscatal.4c03278 (2024).
32 Eggers, A. R. *et al.* Rapid DNA unwinding accelerates genome editing by engineered CRISPR-Cas9. *bioRxiv*, 2023.2012.2014.571777, doi:10.1101/2023.12.14.571777 (2023).
33 Doudna, J. A. The promise and challenge of therapeutic genome editing. *Nature* **578**, 229-236, doi:10.1038/s41586-020-1978-5 (2020).
34 Palermo, G. *et al.* Protospacer Adjacent Motif-Induced Allostery Activates CRISPR-Cas9. *J Am Chem Soc* **139**, 16028-16031, doi:10.1021/jacs.7b05313 (2017).
35 Hou, Z. *et al.* Efficient genome engineering in human pluripotent stem cells using Cas9 from Neisseria meningitidis. *Proceedings of the National Academy of Sciences of the United States of America* **110**, 15644-15649, doi:10.1073/pnas.1313587110 (2013).
36 Kleinstiver, B. P. *et al.* High-fidelity CRISPR-Cas9 nucleases with no detectable genome-wide off-target effects. *Nature* **529**, 490-495, doi:10.1038/nature16526 (2016).
37 Hu, J. H. *et al.* Evolved Cas9 variants with broad PAM compatibility and high DNA specificity. *Nature* **556**, 57-63, doi:10.1038/nature26155 (2018).
38 Lee, J. K. *et al.* Directed evolution of CRISPR-Cas9 to increase its specificity. *Nat Commun* **9**, 3048, doi:10.1038/s41467-018-05477-x (2018).
39 Ma, E., Harrington, L. B., O'Connell, M. R., Zhou, K. & Doudna, J. A. Single-Stranded DNA Cleavage by Divergent CRISPR-Cas9 Enzymes. *Mol Cell* **60**, 398-407, doi:10.1016/j.molcel.2015.10.030 (2015).
40 Nguyen, V. *et al.* Evolutionary drivers of thermoadaptation in enzyme catalysis. *Science* **355**, 289-294, doi:10.1126/science.aah3717 (2017).
41 Saavedra, H. G., Wrabl, J. O., Anderson, J. A., Li, J. & Hilser, V. J. Dynamic allostery can drive cold adaptation in enzymes. *Nature* **558**, 324-328, doi:10.1038/s41586-018-0183-2 (2018).
42 Shmakov, S. *et al.* Diversity and evolution of class 2 CRISPR-Cas systems. *Nat Rev Microbiol* **15**, 169-182, doi:10.1038/nrmicro.2016.184 (2017).
43 Venters, R. A., Farmer, B. T., 2nd, Fierke, C. A. & Spicer, L. D. Characterizing the use of perdeuteration in NMR studies of large proteins: 13C, 15N and 1H assignments of human carbonic anhydrase II. *Journal of molecular biology* **264**, 1101-1116, doi:10.1006/jmbi.1996.0699 (1996).
44 Pervushin, K., Riek, R., Wider, G. & Wüthrich, K. Attenuated T2 relaxation by mutual cancellation of dipole-dipole coupling and chemical shift anisotropy indicates an avenue to NMR structures of very large biological macromolecules in solution. *Proceedings of the National Academy of Sciences of the United States of America* **94**, 12366-12371, doi:10.1073/pnas.94.23.12366 (1997).
45 Tugarinov, V., Kanelis, V. & Kay, L. E. Isotope labeling strategies for the study of high-molecular-weight proteins by solution NMR spectroscopy. *Nat Protoc* **1**, 749-754, doi:10.1038/nprot.2006.101 (2006).
46 Delaglio, F. *et al.* NMRPipe: a multidimensional spectral processing system based on UNIX pipes. *J Biomol NMR* **6**, 277-293, doi:10.1007/bf00197809 (1995).
47 Lee, W., Tonelli, M. & Markley, J. L. NMRFAM-SPARKY: enhanced software for biomolecular NMR spectroscopy. *Bioinformatics* **31**, 1325-1327, doi:10.1093/bioinformatics/btu830 (2015).

48 Keller, R. L. J. *Optimizing the process of nuclear magnetic resonance spectrum analysis and computer aided resonance assignment* Doctoral Thesis thesis, ETH Zürich, (2005).

49 Nerli, S., De Paula, V. S., McShan, A. C. & Sgourakis, N. G. Backbone-independent NMR Resonance Assignments of Methyl Probes in Large Proteins. *Nat. Commun.* **12**, 691 (2021).

50 De Paula, V. S., Dubey, A., Arthanari, H. & Sgourakis, N. G. Dynamic Sampling of a Surveillance State Enables DNA Proofreading by Cas9. *Cell Chem. Biol.* **doi.org/10.1016/j.chembiol.2024.10.001** (2024).

51 Loria, J. P., Rance, M. & Palmer, A. G. A Relaxation-Compensated Carr−Purcell−Meiboom−Gill Sequence for Characterizing Chemical Exchange by NMR Spectroscopy. *Journal of the American Chemical Society* **121**, 2331-2332, doi:10.1021/ja983961a (1999).

52 Bieri, M., d'Auvergne, E. J. & Gooley, P. R. relaxGUI: a new software for fast and simple NMR relaxation data analysis and calculation of ps-ns and µs motion of proteins. *J Biomol NMR* **50**, 147-155, doi:10.1007/s10858-011-9509-1 (2011).

53 Luz, Z. & Meiboom, S. Nuclear Magnetic Resonance Study of the Protolysis of Trimethylammonium Ion in Aqueous Solution—Order of the Reaction with Respect to Solvent. *The Journal of Chemical Physics* **39**, 366-370, doi:10.1063/1.1734254 (1963).

54 Cavanaugh, J. E. & Neath, A. A. The Akaike Information Criterion: Background, Derivation, Properties, Application, Interpretation, and Refinements. *WIREs Comp. Mol. Sci.* **11**, e1460 (2019).

55 Brüschweiler, R., Liao, X. & Wright, P. E. Long-range Motional Restrictions in a Multidomain Zinc-finger Protein from Anisotropic Tumbling. *Science* **268**, 886-889 (1995).

56 Mandel, A. M., Akke, M. & Palmer, A. G. Backbone Dynamics of Escherichia coli Ribonuclease HI: Correlations with Structure and Function in an Active Enzyme. *J. Mol. Biol.* **246**, 144-163 (1995).

57 Fushman, D., Cahill, S. & Cowburn, D. The Main-chain Dynamics of the Dynamin Pleckstrin Homology (PH) Domain in Solution: Analysis of 15N Relaxation with Monomer/Dimer Equilibration. *J. Mol. Biol.* **266**, 173-194 (1997).

58 Orekhov, V. Y., Korzhnev, D. M., Diercks, T., Kessler, H. & Arseniev, A. S. 1H-15N NMR Dynamic Study of an Isolated α-helical Peptide (1-36)bacteriorhodopsin Reveals the Equilibrium Helix-coil Transitions. *J. Biomol. NMR* **14**, 345-356 (1999).

59 Korzhnev, D. M., Billeter, M., Arseniev, A. S. & Orekhov, V. Y. NMR Studies of Brownian Tumbling and Internal Motions in Proteins. *Prog. NMR Spectros.* **38**, 197-266 (2001).

60 Zhuravleva, A. V. *et al.* Gated Electron Transfers and Electron Pathways in Azurin: A NMR Dynamic Study at Multiple Fields and Temperatures. *J. Mol. Biol.* **342**, 1599-1611 (2004).

61 Tjandra, N., Feller, S. E., Pastor, R. W. & Bax, A. Rotational Diffusion Anisotropy of Human Ubiquitin from N-15 NMR Relaxation. *J. Am. Chem. Soc.* **117**, 12562-12566 (1995).

62 Kabsch, W. XDS. *Acta Crystallogr D Biol Crystallogr* **66**, 125-132, doi:10.1107/s0907444909047337 (2010).

63 Winn, M. D. *et al.* Overview of the CCP4 suite and current developments. *Acta Crystallogr D Biol Crystallogr* **67**, 235-242, doi:10.1107/s0907444910045749 (2011).

64 Liebschner, D. *et al.* Macromolecular structure determination using X-rays, neutrons and electrons: recent developments in Phenix. *Acta Crystallogr D Struct Biol* **75**, 861-877, doi:10.1107/s2059798319011471 (2019).

65 Emsley, P., Lohkamp, B., Scott, W. G. & Cowtan, K. Features and development of Coot. *Acta Crystallogr D Biol Crystallogr* **66**, 486-501, doi:10.1107/s0907444910007493 (2010).

66 Sinha, S., Pindi, C., Ahsan, M., Arantes, P. R. & Palermo, G. Machines on Genes through the Computational Microscope. *J. Chem. Theor. Comput.* **19**, 1945-1964 (2023).

67 Saha, A. *et al.* An Alpha-helical Lid Guides the Target DNA Toward Catalysis in CRISPR-Cas12a. *Nat. Commun.* **15**, DOI: 10.1038/s41467-41024-45762-41466 (2024).

68 Arantes, P. R. *et al.* Dimerization of the Deaminase Domain and Locking Interactions with Cas9 Boost Base Editing Efficiency in ABE8e. *Nucl. Acids Res.* **52**, 13931-13944 (2023).

69 Sinha, S. *et al.* Unveiling the RNA-mediated Allosteric Activation Discloses Functional Hotspots in CRISPR-Cas13a. *Nucl. Acids Res.* **52**, 906-920 (2024).

70 Tian, C. *et al.* f19SB: Amino-Acid-Specific Protein Backbone Parameters Trained against Quantum Mechanics Energy Surfaces in Solution. *J. Chem. Theor. Comput.* **16**, 528-552 (2019).

71 Galindo-Murillo, R. *et al.* Assessing the Current State of Amber Force Field Modifications for DNA. *J. Chem. Theor. Comput.* **12** (2016).

72 Zgarbova, M. *et al.* Refinement of the Cornell et al. Nucleic Acids Force Field Based on Reference Quantum Chemical Calculations of Glycosidic Torsion Profiles. *J. Chem. Theor. Comput.* **7**, 2886-2902 (2011).

73 Jorgensen, W. L., Chandrasekhar, J., Madura, J. D., Impey, R. W. & Klein, M. L. Comparison of Simple Potential Functions for Simulating Liquid Water. *J. Chem. Phys.* **79**, 926-935 (1983).

74 Case, D. A. *et al.* The Amber Biomolecular Simulation Programs. *J. Comput. Chem.* **26**, 1668-1688, doi:10.1002/jcc.20290 (2005).

75 Mongan, J., Simmerling, C., McCammon, J. A., Case, D. A. & Onufriev, A. Generalized Born Model with a Simple, Robust Molecular Volume Correction. *J. Chem. Theor. Comput.* **3**, 156-169 (2007).

76 Nguyen, H., Pérez, A., Bermeo, S. & Simmerling, C. Refinement of Generalized Born Implicit Solvation Parameters for Nucleic Acids and their Complexes with Proteins. *J. Chem. Theor. Comput.* **11**, 3714-3728 (2015).

77 Nguyen, H., Roe, D. R. & Simmerling, C. Improved Generalized Born Solvent Model Parameters for Protein Simulations. *J. Chem. Theor. Comput.* **9**, 2020-2034 (2013).